Crepe Cake Structured Layered Double Hydroxide/Sulfur /Graphene as a Positive Electrode Material for Li-S Batteries

Shengtang Liu,[a] Xiuying Zhang,[b] Shitao Wu,[c] Xi Chen,[a] Xiaojing Yang,[a] Wenbo Yue,[a] Jing Lu,*[b] and Wuzong Zhou*[c]*

[a] Beijing Key Laboratory of Energy Conversion and Storage Materials
College of Chemistry, Beijing Normal University, Beijing 100875 (China)

[b] State Key Laboratory for Mesoscopic Physics and Department of Physics
Peking University, Beijing 100871 (China)

[c] School of Chemistry, University of St Andrews
St Andrews, Fife KY16 9ST (UK)

ABSTRACT

Solving the polysulfide shuttle problem is one of the core challenges for industrialization of lithium-sulfur batteries. In this work, a triphasic composite of layered double hydroxide (LDH)/sulfur/reduced graphene oxide with a crepe cake like structure is designed and fabricated as a positive electrode material for lithium-sulfur batteries. Sulfur nanoparticles are embedded in the interlayer space of the composite, and thus are well protected physically *via* three-dimensional wrapping and chemically *via* strong interaction of LDH nanoflakes with lithium polysulfides, such as ionic bonds and S-H hydrogen bonds. In addition, the flexible lamellar structure of the composite with soft graphene layers can tolerate the volume expansion of sulfur during lithiation as well as facilitate ionic permeability and electron transport, which is favorable for the redox reactions of polysulfide. The present work shed light on the future development and industrialization of lithium-sulfur batteries.

KEYWORDS: crepe cake structure, graphene, layered double hydroxide, sulfur, lithium-sulfur batteries

With the growing demand for energy sources, lithium-ion batteries can no longer meet the requirements of energy supply equipment. Lithium-sulfur (Li-S) batteries are deemed as promising energy storage devices to replace lithium-ion batteries, due to their high theoretical specific energy (2600 Wh kg^{-1}, obtained by calculating the total mass of the sulfur and lithium electrodes), low cost and environmental benignity.[1,2] The lithium storage mechanism in the Li-S batteries is a multi-electron transfer process ($16Li^+ + S_8 + 16e^- = 8Li_2S$), and thus a high theoretical capacity of sulfur (1675 mA h g^{-1}, calculated by using the formula: nF/3.6M, where M is molar mass of S_8 when n=16, or M is molar mass of S when n=2) is achieved.[3,4] However, some drawbacks impede the practical applications of Li-S batteries. For example, the poor electrical conductivity of sulfur slows down the reaction rate of sulfur with Li^+ ions, especially for bulk sulfur, and the severe volume change of sulfur upon lithiation could destroy the structure of positive electrode, resulting in the performance degradation.[5,6] More seriously, the dissolved long-chain lithium polysulfides (Li_2S_x, $4 \leq x \leq 8$) can migrate through the separator and react with the lithium negative electrode, leading to loss of active sulfur, low Coulombic efficiency, significant polarization and rapid capacity fading.[7,8] Therefore, this undesired "shuttle effect" becomes the pivotal problem that limits the industrialization of lithium-sulfur batteries.

Developing functional host materials for loading sulfur is an effective way to overcome these drawbacks. Mesoporous carbon materials, such as CMK-3, were considered as sulfur supports at first because sulfur particles could be evenly distributed in the mesopores of CMK-3 and the volume expansion of sulfur could be effectively tolerated.[9] However, the interaction between non-polar carbon skeleton and polar polysulfides was too weak to suppress the shuttle effect. Thus polymer encapsulation was adopted later to stop the diffusion of polysulfides. More recently, polar inorganic compounds[10,11] such as metal oxides,[12] metal sulfides,[13,14] metal nitrides,[15,16] and even heteroatom doping carbon materials[17] were considered as sulfur host materials owing to the chemical interactions with lithium polysulfides (LiPS), including polar-polar interaction[18,19] or Lewis acid-base interaction.[20,21] Theoretical calculations also confirmed that weak chemical bonds formed between LiPS and these polar materials,[22] relying on the interactions of lithium with non-metal atoms (*e.g.*, Li···S,[14] Li···O,[23,24] Li···N[25]) and sulfur with metal atoms (M···S).[26] Unfortunately, this kind of delicate and infirm force could not effectively prevent the polysulfide diffusion.

Considering that long-chain LiPS are anionic compounds and inevitably dissolve in many electrolytes, the capture capability for LiPS would be greatly increased through building an electrostatic interaction with positively charged host materials and even forming ionic bonds. Layered double hydroxides (LDHs) are a class of ionic lamellar compounds which consist of positively charged metal hydroxide layers and charge-balancing anions in the interlayer regions.[27] The LDHs with positively charged layers are probably ideal two-dimensional (2D) host materials which are able to capture LiPS by an electrostatic interaction besides a polar-polar interaction. More importantly, the layers of LDHs possess lots of hydroxyl groups on the surface, which can further strengthen the interaction between LDHs and LiPS,[28,29] by forming hydrogen bonds (O−H···S). Although the S-H hydrogen bond is weaker than normal hydrogen bond, in view of the number of hydroxyl groups on the layers, forming S-H hydrogen bonds is also beneficial for immobilization of LiPS during cycling. Consequently, LDHs are very worthy to be studied in-depth as advanced sulfur host materials for Li-S batteries.

Construction of functional sulfur hosts also strongly influences the electrochemical performance of the sulfur positive electrode.[30] On one hand, bulk LDHs cannot form strong interactions with LiPS because of its low surface area and lack of enough amount of active hydroxyl groups. LDH nanosheets in exfoliated state are much desired for the purpose of forming strong ionic bonds and S-H hydrogen bonds with LiPS. However, this state is unstable and tends to rearrange into layered solids without formamide protection. Constructing highly dispersed LDH nanoflakes with stable structure is very important for the application of LDHs as sulfur hosts. On the other hand, the problems of the low conductivity and the volume expansion of sulfur during lithiation still need to be solved. Integration with conductive and flexible materials such as graphene not only immobilizes LDH nanoflakes to avoid their stacking, but also improves the electrical conductivity of LDH-based host as well as endures the stress induced by the volume expansion of sulfur. An ideal structure for the sulfur positive electrode is all round package of sulfur, *i.e.*, a sealing structure that only allows lithium ions and some small organic molecules to enter and exit, which avoid the expose of sulfur to electrolyte and the dissolution of LiPS into electrolyte.

Up to date, several methods for wrapping sulfur have been developed. Sulfur is encapsulated within elaborately designed materials with special structures such as porous structures, nanotubes, or hollow spheres.[22] However, there is a contradiction that sulfur is loaded on these hosts by a melt-impregnation method, and naturally withdraws freely from these hosts during lithiation. A

reasonable approach for encapsulated sulfur is *in situ* growth or coating of polar inorganic compounds on the surface of sulfur, such as the reported yolk-shell structured sulfur@TiO_2,[12] and core-shell structured sulfur@carbon-black@$Ni_3(NO_3)_2(OH)_4$.[29] Nevertheless, owing to the difficulties in controlling the experimental conditions, the particle size of the encapsulated sulfur was too large and the structural homogeneity was uncontrollable, leading to a low reaction kinetics and insufficient usage of sulfur. In addition, the spherical morphology of these sulfur@hosts particles goes against the tap-density of the sulfur positive electrode. In view of these disadvantageous factors, *in situ* formation of sulfur nanoparticles within lamellar structured multi-functional composite hosts may be an ideal all-round packaged sulfur positive electrode for Li-S batteries.

Herein, we designed an all-round packaged sulfur positive electrode with good electrochemistry performance for Li-S batteries. The lamellar structure of the material is constructed by an assembly of exfoliated NiAl-LDH nanosheets and sulfur decorated reduced graphene oxide (rGO) nanosheets. The former has a strong capture capability for LiPS and the use of rGO in the latter can improve the electrical conductivity of the composite.[32-34] Sulfur nanoparticles are well-encapsulated in between LDH and rGO and the overall structure of LDH/S/rGO looks crepe cake like. This structure allows lithium ions to transfer through the interlayer space and to react with embedded sulfur nanoparticles, but LiPS are unable to escape from the structure due to the closed space in the composite and strong interactions with the LDH nanoflakes, maximally suppressing the shuttle effect. This developed crepe cake like structure with encapsulated nanoscale sulfur particles provides a design concept of high performance sulfur positive electrode materials.

RESULTS AND DISCUSSION

Figure 1 shows the experimental procedure of the synthesis of the LDH/S/rGO hybrid through self-assembly of the 2D charged nanosheets of exfoliated NiAl-LDH and sulfur-decorated rGO. The details of experiments are given in the Experimental Section.

The starting takovite-type material, $Ni_6Al_2(OH)_{16}CO_3{\cdot}4H_2O$, has a rhombohedral unit cell with a = 0.302, c = 2.22 nm. The structure is constructed by LDH of metal cation (Ni^{2+}, Al^{3+}) layer sandwiched by two hydroxide layers, and these LDH layers are separated by CO_3^{2-} anion layers. The material is designated LDH/CO_3. Since each unit cell contains three LDH layers, packing along the c axis, the interlayer space is indicated by $d_{(003)}$, which is 0.74 nm (Figure S1).

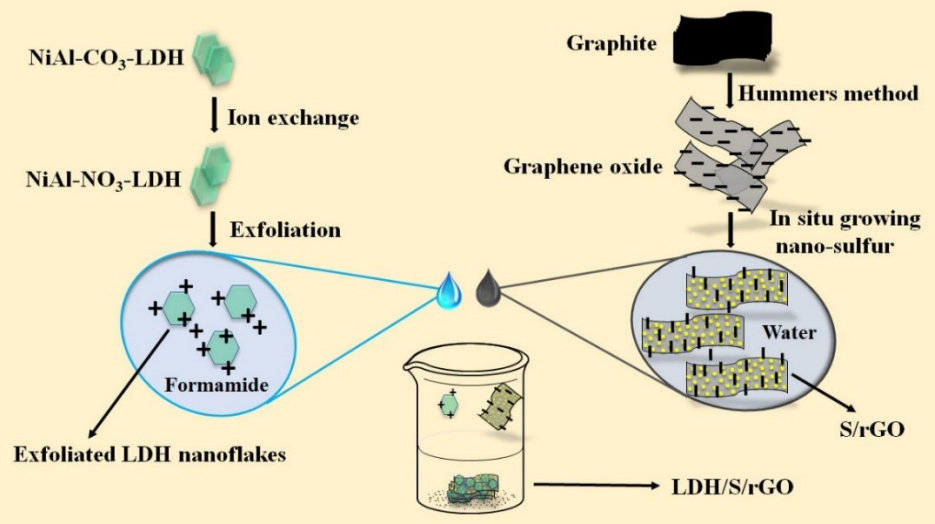

Figure 1. Illustration of synthesis route for the LDH/S/rGO hybrid.

The LDH/CO_3 specimen underwent a phase transformation to LDH/NO_3 *via* an ion exchange of CO_3^{2-} by NO_3^-. The interlayer space, $d_{(003)}$, increased from 0.74 to 0.87 nm, while the structure in the ab planes of LDH maintained intact, as indicated by the X-ray diffraction (XRD) results with insignificant shifts of the (012) and (110) peaks (Figure S1). The weakened interlayer interaction and the enlarged interlayer spacing are conducive to the exfoliation of LDH layers in the formamide solution under mechanical shaking.

In a parallel experiment, sulfur nanoparticles *in situ* precipitated on the surface of graphene oxide (GO) nanosheets, which were obtained by chemical exfoliation of graphite. Meanwhile, GO was reduced to rGO during the growth process of sulfur (Figure 1). Scanning electron microscopy (SEM) images show that the dried particles of S/rGO are irregularly-shaped aggregates of the graphene nanosheets with evenly distributed sulfur as detected by energy dispersive X-ray spectroscopic (EDX) elemental mapping (Figure S2).

The obtained LDH and sulfur-decorated rGO (S/rGO) colloidal dispersions were simultaneously added into a formamide solvent. These two oppositely charged nanosheets self-assembled into an alternatively stacked superstructure with electrostatic interactions. Soon afterwards, a certain amount of deionized water was added into the formamide suspension in order to enhance precipitation of LDH/S/rGO. The particle size of NiAl-LDHs can be easily tuned by controlling nucleation and growth processes. Thus relatively small nanoflakes of LDH were prepared and used

as a “rivet” in the hybrid to connect the rGO layers and form a modulated structure of LDH/S/rGO (Figure S3).

Figure 2a shows XRD pattern of LDH/S/rGO. The broad peaks can be indexed to the takovite-type structure with the $d_{(003)}$ value increasing to 1.04 nm. The another set of diffraction peaks, can be indexed to crystalline sulfur,[8] which has an orthorhombic unit cell with a = 1.045, b = 1.284, c = 2.446 nm. The XRD result provides unambiguous evidence for the formation of ABAB stacking of the LDH and S/rGO sheets. Figure S4 shows high resolution transmission electron microscopic (HRTEM) profile images of LDH/S/rGO particles, revealing the microstructures of packing. It is confirmed that S nanoparticles are indeed embedded in the interlayer space of LDH, presented as dark regions. It is also in certain that the distribution of the S nanoparticles are not even and the particle size is not uniform. Consequently, the LDH layers are no longer flat, but modulated due to the insertion of the sulfur nanocrystallites. The continuity of the LDH layers can be broken when they meet large S particles. The XRD pattern in Figure 2a was a result of many regions with different interlayer *d*-spacings, since the overall structure is crepe cake like without a long range ordering or a well-defined 3D unit cell. This construction of LDH/S/rGO realizes all-round package for sulfur, and only allows the access of lithium ions, but avoids loss of sulfur.

Further characterization using electron microscopy was performed. The produced LDH/S/rGO are irregular bulk particles. High magnification SEM images on a face of a LDH layer show many lumps, 10 to 20 nm in diameter (Figure 2b). From the TEM study, a typical selected area electron diffraction (SAED) pattern viewing down the LDH face is shown in Figure 2c. The diffraction rings can be indexed to either LDH or sulfur crystals according to the measured *d*-spacings, *e.g.*, d_A = 0.115, d_B = 0.125, d_C = 0.150 nm, corresponding to the (208), (205), (110) planes of the takovite-type structure, d_D = 0.205, d_E = 0.242 nm, corresponding to the (00 12) and (404) planes of the S nanocrystals, respectively. The smallest ring with d_F = 0.260 nm could be indexed to the (400) planes of S and the (100) planes of LDH. It is noted that the {100} diffraction of the original takovite structure with space group R-3m is systematic absent. However, the ordering along the c axis was lost when the LDH sheets re-stacked with S/rGO, the {100} diffraction peaks were not absent. This SAED pattern is basically a pattern of polycrystalline specimen. However, there are six maxima in the ring of C, forming a hexagonal pattern, which can be indexed to the {110} planes of the LDH derived structure, indicating that many LDH sheets share the same orientation. The appearance of weak spots in that ring implies that some of the LDH plates are randomly

orientated by rotating around the [001] axis. The co-existence of the (208) and (205) rings indicate that some LDH plates are no longer perpendicular to the incident electron beam, but tilted with different angles. The results are consistent with the crepe cake like structure, where the original LDH layers are modulated.

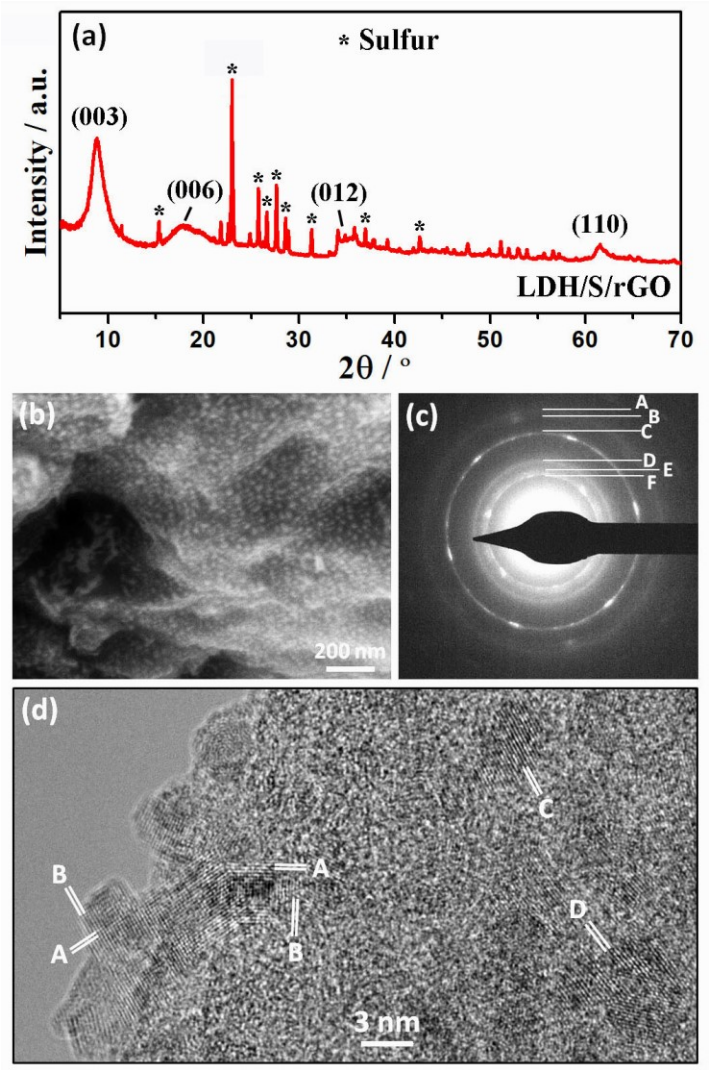

Figure 2. (a) XRD pattern of the product LDH/S/rGO. The marked peaks are indexed to a takovite-like structure with $d_{(003)}$ being 1.04 nm. The peaks marked with 'star' are from crystalline sulfur. (b) SEM image of a LDH/S/rGO particle viewed down a face of LDH. (c) SAED pattern recorded from a LDH/S/rGO particle when viewing down the [001] direction of the LDH component. The diffraction rings can be indexed to either LDH or S crystals. (d) HRTEM image of the same particle. The fringes of the nanocrystals can be indexed to the S structure.

The HRTEM image of an edge of a LDH/S/rGO particle in Figure 2d shows some sulfur nanocrystallites embedded in the particle and some exposed on the side surface. The measured *d*-spacings from the nanocrystallites show d_A = 2.04, d_B = 2.13, $d_C \approx d_D$ = 2.41 nm, and the corresponding fringes can be indexed to the (440), (2-2 10), (404) planes of the sulfur structure. The sulfur crystal sizes fall in a range from ca. 2 nm to 5 nm, which are much smaller than the lumps observed in the SEM image in Figure 2b. The latter are actually the distorted areas induced by the sulfur nanocrystallites underneath the surface LDH layer. The lattice fringes of LDH are not visible on the image due to their small values and mis-orientation.

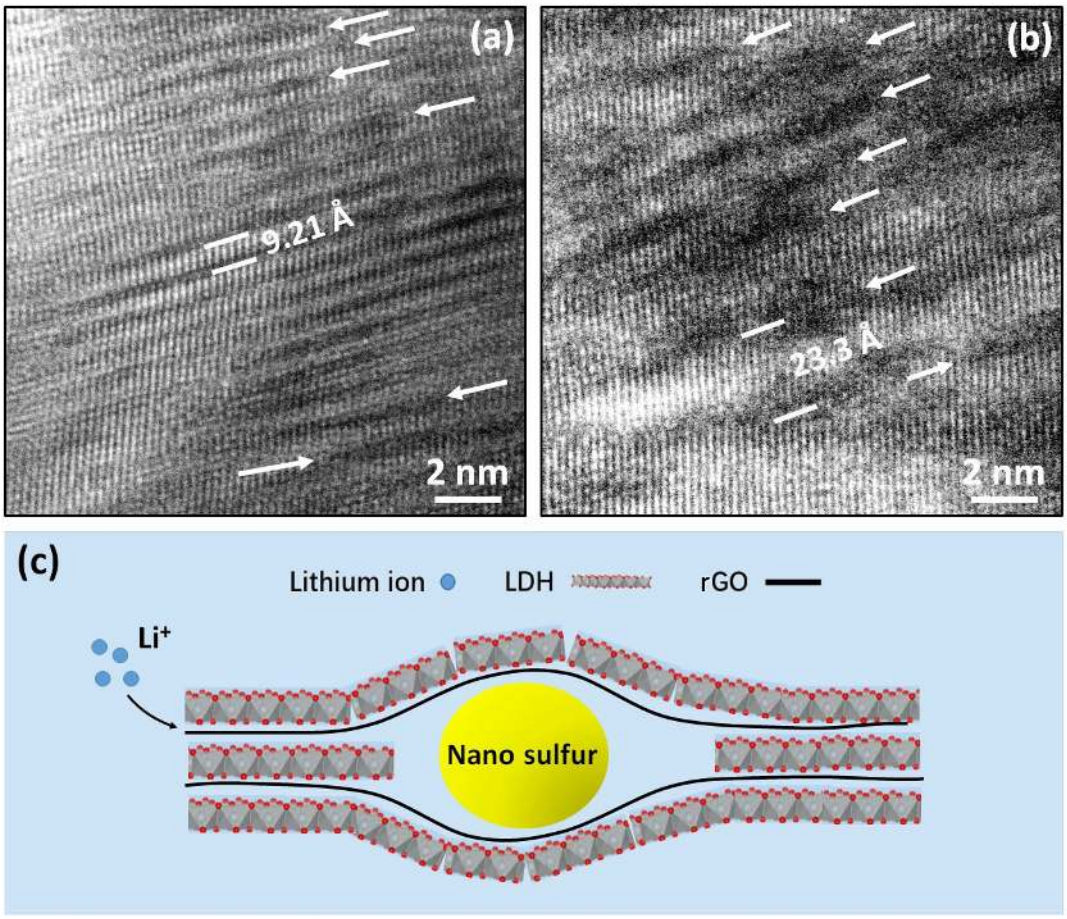

Figure 3. (a, b) Enlarged HRTEM images of two selected areas on the image of Figure S4(a), showing sulfur insertion between the LDH layers as indicated by the arrows. (c) A schematic drawing to show a sulfur nanocrystal embedded in the LDH layers.

Two selected areas in the HRTEM image (Figure S4a) are enlarged and shown in Figure 3. The layered structure in Figure 3a is relatively more regular and the interlayer distance, corresponding to the (003) *d*-spacing of the unit cell, is 0.921 nm. This value corresponds to the *d*-spacing of the (003) planes of S-free LDH/rGO. The thicker layers with light contrast are the images of the LDH layers and the thin dark layers are rGO. Some arrows in Figure 3a point to some thicker dark areas in the rGO locations, indicating existence of very small sulfur nanoparticles. The local interlayer spacing is therefore expanded and the LDH layers are modulated. Figure 3b is the HRTEM image of the second area where larger sulfur particles are visible, indicated by the arrows. Because more sulfur particles are overlapped viewing down this profile direction of the crepe cake like particle, no lattice fringes of sulfur nanocrystallites were observed. Figure 3c shows a schematic drawing of a sulfur nanocrystal embedded in the LDH layers. When the material is used in Li-S batteries, lithium can easily migrate through the interlayer space, but LiPS cannot. The shutter effect is therefore minimized for a high energy density of batteries. EDX elemental mapping of the LDH/S/rGO particles show evenly distributed Ni, Al, O, C, and S (Figure S5).

The surface chemical states of LDH/S/rGO and the interaction among rGO, sulfur and LDH were studied by X-ray photoelectron spectroscopy (XPS), in which the peaks of Al 2p, S 2p, C 1s, O 1s and Ni 2p are detected in the XPS survey spectrum (Figure 4a), indicating the components of the composite. The LDH/S/rGO exhibits strong chemical interaction between sulfur and the LDH/rGO host, as revealed by the high-resolution XPS spectra. Figure 4b shows the S $2p_{3/2}$ and $2p_{1/2}$ doublet with an energy separation of 1.2 eV and intensity ratio of 2:1. The binding energy of S $2p_{3/2}$ peak is 163.6 eV, slightly lower than that of elemental sulfur (164.0 eV). The peak shift reflects the formation of C-S bonds between sulfur and rGO because the elemental electronegativity of S is higher than that of C. In the same vein, the signal detected at 164.2eV represents the existence of O-S bonds due to the higher electronegativity of O.[35] The small shoulder at ~169 eV is ascribed to the sulphate species derived from the residual precursor or formed by sulfur oxidation in air.[36]

Figure 4c,d show the high-resolution Ni 2p and Al 2p XPS spectra of LDH/CO_3 and LDH/S/rGO. The XPS spectra of the former show two peaks at 856.2 and 873.8 eV, which are assigned to the Ni $2p_{3/2}$ and Ni $2p_{1/2}$ doublet with two satellites.[37,38] The peak of Al 2p is located at 74.3 eV, indicating the formation of Al-OH.[39] In comparison, the peaks of Ni 2p and Al 2p in the spectra of LDH/S/rGO shift to higher bonding energies, implying stronger interactions between

LDH and rGO. The XPS peak shift of elements is generally related to the dispersion state, chemical valence and chemical micro-circumstances of composites.[40] Accordingly, the XPS results indicate the strong interactions between LDH and rGO such as the electrostatic interaction between the positively charged LDH nanoflakes and the negatively charged rGO nanosheets, as well as hydrogen bonds (O-H) between the carboxylic/hydroxyl groups of rGO and hydroxyl groups of LDHs. Although GO is reduced to rGO,[41] confirmed by XPS and Raman analyses (Figure S6), some carboxylic/hydroxyl groups still remain on the surface of rGO.

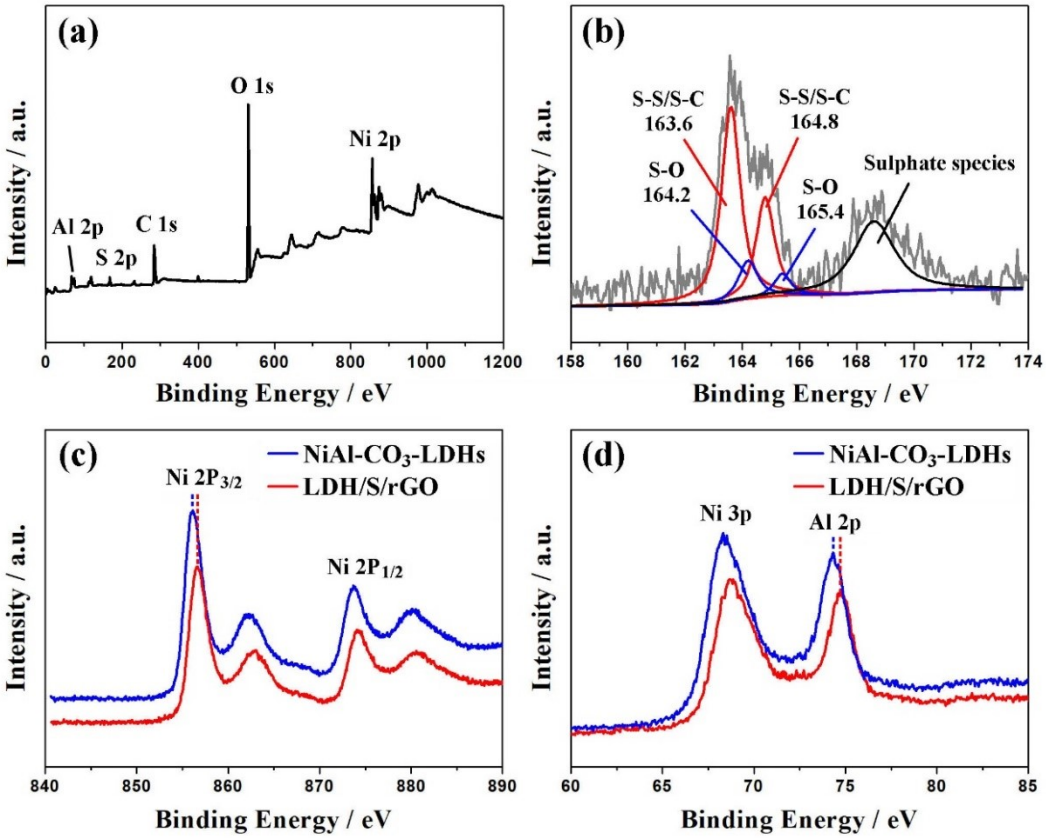

Figure 4. (a) XPS survey and (b) high-resolution S 2p XPS spectra of LDH/S/rGO. High-resolution (c) Ni 2p and (d) Al 2p XPS spectra of LDH/CO_3 and LDH/S/rGO.

Using an established method reported in the literature,[42] the sulfur content in LDH/S/rGO is detected as ~61.7 wt% based on the thermogravimetric analysis (TGA) of LDH/S/rGO and LDH/rGO (Figure S7a). The sulfur loading of LDH/S/rGO is definitely limited by the self-assembly process and the superlattice structure of LDH/rGO. Loading more sulfur would cause

the exposure of sulfur nanoparticles as well as the structural damage of LDH/S/rGO. Nevertheless, the good part is that this kind of all-round packaged structure can prevent the shuttle of LiPS to the greatest extent. For the comparison of electrochemical performance, the sulfur content of S/rGO is ~60.9 wt% by control (Figure S7b).

Electrochemical measurements reveal the structural superiority of LDH/S/rGO for Li-S batteries. To explore the related mechanism, cycle voltammograms (CVs) of LDH/S/rGO and S/rGO were recorded at a scan rate of 0.2 mV s^{-1}. When scanning between 1.5 and 3.2 V, S/rGO (Figure 5a) shows two typical reduction peaks at 2.23 and 1.96 V, which are assigned to the multistep reduction, from solid sulfur to soluble long-chain LiPS and finally to the end-product Li_2S_2/Li_2S. In the subsequent anodic process, the peak at 2.51 V results from the reversible oxidation from Li_2S/Li_2S_2 to long-chain LiPS and eventually back to solid sulfur.[43] Compared to S/rGO, the redox peaks of LDH/S/rGO shift to 2.26/2.02 and 2.45 V, respectively. Such peak shift illustrates that the electrochemical polarization is effectively suppressed by the introduction of LDH nanoflakes.[44,45] The lithiation and delithiation of sulfur at lower overpotentials can be attributed to the fast reaction kinetics within the interlayers of LDH/rGO. The redox reactions of sulfur are activated by LDH, which exhibits high catalytic activity, similar to those of noble metal Pt[2] or other catalysts such as FeP[46] and MnO_2.[47] More interestingly, the strong and sharp peaks of LDH/S/rGO are also correlated with the fast conversion of sulfur to LiPS on LDHs. Figure 5b shows the galvanostatic charge/discharge profiles of LDH/S/rGO and S/rGO at a constant C rate of 0.2 C. For LDH/S/rGO, two discharge plateaus at 2.28 and 2.10 V and two charge plateaus at 2.25 and 2.33 V correspond to the multistep lithiation-delithiation processes. The polarization of LDH/S/rGO (ΔE = 0.23 V) is lower than that of S/rGO (ΔE = 0.32 V), consistent with the CV results. The specific energy of the cell made by using LDH/S/rGO as the positive electrode, and metal lithium as the negative electrode is calculated based on the integral area of the discharge curve of LDH/S/rGO. The value is ~2030 Wh kg^{-1}. Considering that the theoretical specific energy of Li-S batteries is 2600 Wh kg^{-1}, the energy efficiency of the cell is about 78.1%. In general, the high discharge voltage and capacity of the LDH/S/rGO positive electrode is beneficial to boost the overall specific energy of Li-S batteries.

To gain deeper insights into the catalytic effect of LDH on the redox kinetics of LiPS, a symmetrical cell was assembled by using LDH/rGO or rGO as identical electrodes. The Li_2S_6-containing electrolyte was prepared according to the literature.[41] Polarization curves (Figure 5c)

show that either LDH/rGO or rGO has weak current response in Li_2S_6-free electrolyte, but in Li_2S_6-containing electrolyte, LDH/rGO exhibits stronger current response than rGO, suggesting that LDH can accelerate the redox reaction of LiPS.

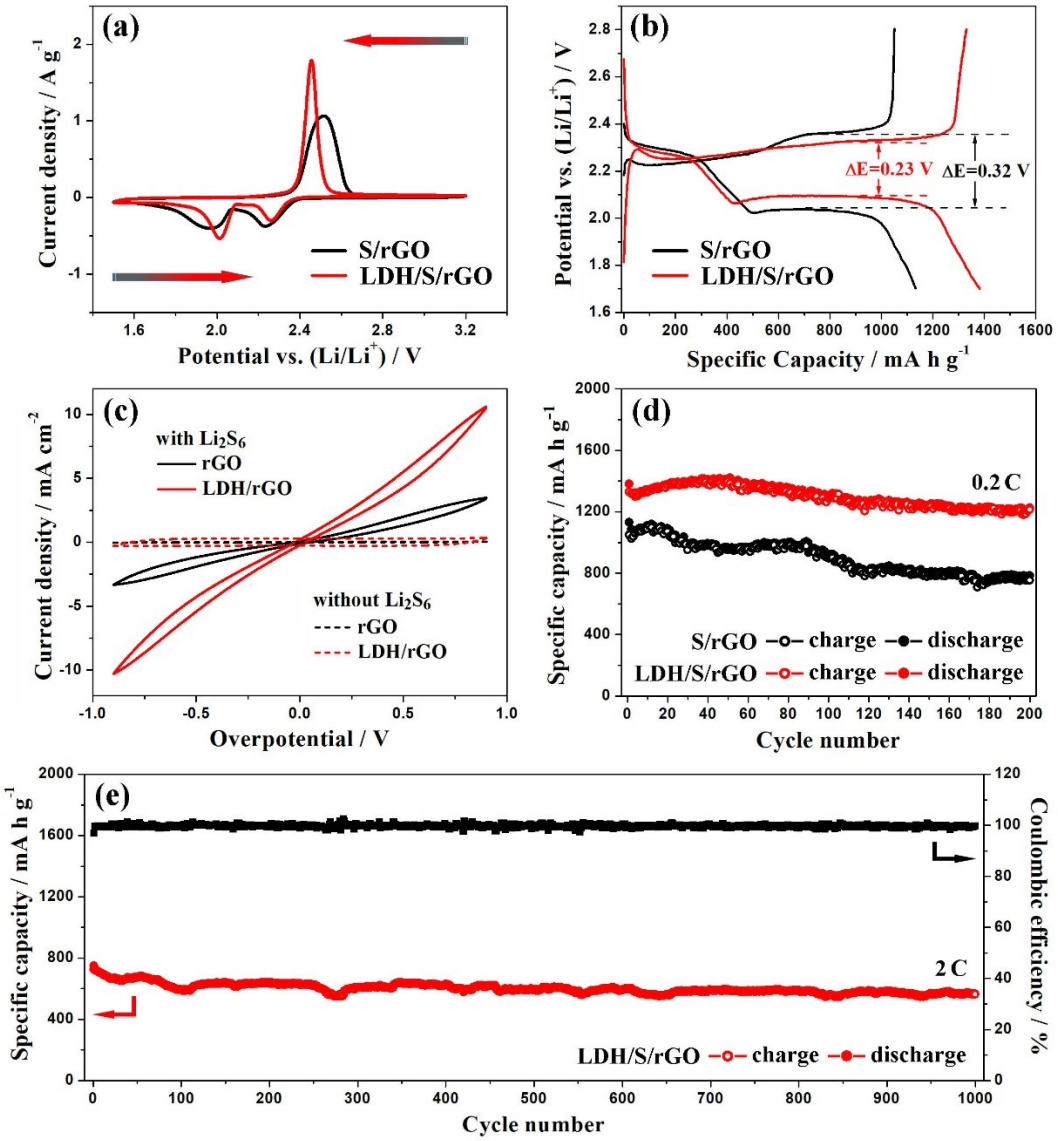

Figure 5. (a) CVs and (b) potential profiles of LDH/S/rGO and S/rGO. (c) Polarization curves of the symmetrical battery with identical electrode. (d) Cycle performance of LDH/S/rGO and S/rGO at 0.2 C. (e) Long cycle performance of LDH/S/rGO at 2 C.

Galvanostatic measurements were subsequently carried out to study the cycling and rate performances. LDH/S/rGO exhibits good cycling stability and a high reversible capacity of 1226

mA h g^{-1} at 0.2 C after 200 cycles (Figure 5d). On the contrary, the reversible capacity of S/rGO decreases evidently upon cycling process due to a severe shuttle effect, and only 783 mA h g^{-1} is achieved at 0.2 C after 200 cycles. It is worth noting that the capacity of LDH/S/rGO gradually increases after several initial cycles, which can be attributed to a self-activity process.[12,29,41] Although lithium ions are allowed to transfer through the interlayer space of LDH/S/rGO, the reaction with sulfur nanoparticles located deeply is restricted by the structure of LDH/S/rGO, and these sulfur would be gradually activated with the intercalation of lithium ions. LDH/S/rGO also displays better rate performance than S/rGO (Figure S8), demonstrating the fast charge and discharge capability of LDH/S/rGO. According to the stability tests at high C rate (Figure 5e), after 1000 cycles, the reversible capacity of LDH/S/rGO is maintained at 566 mA h g^{-1} at 2 C with a capacity retention of 80% (vs. the second reversible capacity), and the Coulombic efficiency reaches up to above 99.5%. As a proof of concept, the devices with high areal sulfur loading (4.2 mg cm^{-2}) (Figure S9) were also measured to meet the basic requirements of commercialized production of Li-S batteries. LDH/S/rGO shows a high capacity of 882 mA h g^{-1}, namely 3.7 mA h cm^{-2} at 0.5 C after 200 cycles, indicating a great application prospect.

The morphology and structure of LDH/S/rGO after 500 cycles were observed by TEM. It is clearly observed that small Li_2S nanoparticles are homogeneously distributed on the surface of rGO without any aggregation (Figure S10), illustrating that LDHs induce the formation and dispersion of Li_2S during cycling. In addition, according to the position of Li_2S, it is inferred that the soluble LiPS are confined to the crepe cake like structure of LDH/LiS_x/rGO, and the shuttle effect is accordingly suppressed. To prove this point, TEM-EDX analyses of LDH/S/rGO and S/rGO after 200 cycles and in charged states were performed. TEM-EDX mapping images of LDH/S/rGO (Figure S11) indicate that sulfur is still uniformly distributed within LDH/rGO after long-term cycling and importantly, the point density of sulfur element is much higher on LDH/rGO than that on rGO (Figure S12), validating that the structure of LDH/S/rGO can effectively prevent the loss of sulfur during the charge and discharge processes.

To investigate the optimal ratio of LDH and rGO to form all-round packaged structure for accommodating sulfur, LDH/S/rGO with weight ratios of LDH/rGO (1:2) and (2:1) were synthesized. It is found that the XRD pattern of LDH/S/rGO (2:1) (Figure S13a) is very similar to that of LDH/S/rGO (1:1) (Figure 2a). The peaks related to the LDH structure are prominent in the XRD pattern of LDH/S/rGO (2:1), but are very weak from LDH/S/rGO (1:2) (Figure S13b),

demonstrating that the layered structure in LDH/S/rGO is more regular when the LDH component increases. The electrochemical performance of LDH/S/rGO with different LDH : rGO ratios is subsequently measured (Figure S14). LDH/S/rGO (1:1) shows stable cyclic performance at 0.5 C, with a reversible capacity of 1203 mA h g^{-1} after 120 cycles. In contrast, LDH/S/rGO (1:2) shows a similar cyclic performance at the early stage, but the capacity decreases dramatically after 80 cycles and a lower capacity of 982 mA h g^{-1} is observed after 120 cycles. The decreased LDH component results in dissolution of LiPS and the loss of active sulfur. On the other hand, a low content of rGO in LDH/S/rGO (2:1) leads to an increased capacity with the increase of cycle number. However, its capacity is only 597 mA h g^{-1} after 120 cycles, much lower than that of LDH/S/rGO (1:1). Although the increased LDH regions can effectively prevent the shuttle of LiPS, the migration of Li^+ in the bulk sample becomes more difficult and the low electrical conductivity of LDHs leads to a decline in the electrochemical performance of LDH/S/rGO (2:1). Consequently, the ratio of LDH : rGO is critical to the electrochemical performance.

To reveal the capture capability of LiPS on LDH nanoflakes, the adsorption experiment of Li_2S_4 in LDH colloidal solution was performed. Block LDHs were first exfoliated into LDH nanoflakes in formamide. Compared to pure formamide, the exfoliated LDH colloidal solution presents evident Tyndall phenomenon (Figure 6a). The Li_2S_4-containing electrolytes were added into the pure formamide, LDH colloidal and LDH block suspensions (Figure 6b), respectively. It was found that the transparent formamide turned yellow after addition of Li_2S_4, whereas the blue LDH colloidal suspension turned brown in 1 min (Figure 6c), and then changes to homogenized black suspension after 5 min (Figure 6d). Subsequently, black LDH solid precipitates are formed in the solution and this precipitation is almost completed after 40 min (Figure 6e). After 12 h (Figure 6f), the solution is completely transparent. The colorless solution shows that Li_2S_4 is entirely adsorbed by exfoliated LDH nanoflakes. The color with addition of Li_2S_4 of the parallel group (block LDH suspension) is similar to that of pure formamide. 12 h later, the yellow color of the block LDHs suspension becomes lighter, implying that block LDHs can also adsorb LiPS, but the adsorption efficiency is significantly lower in comparison with the exfoliated LDH nanoflakes, regardless of adsorption rate and adsorption capacity.

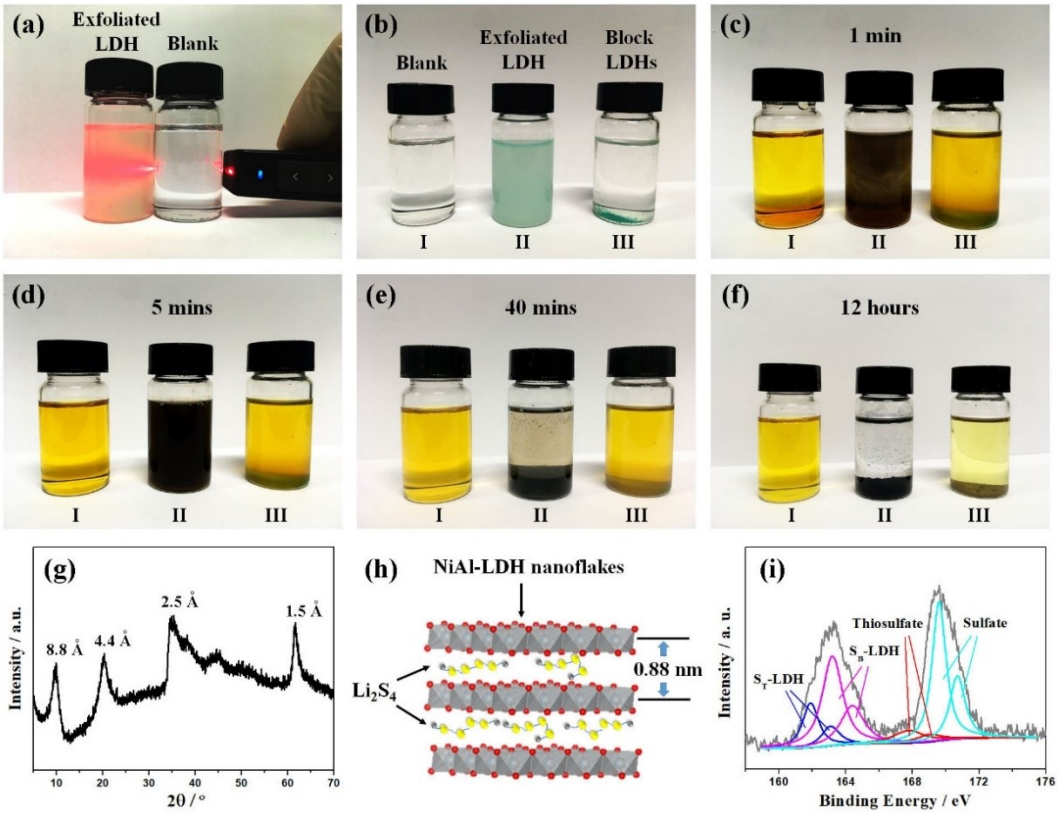

Figure 6. (a) Digital picture of exfoliated LDH in formamide with Tyndall phenomenon. (b-f) Digital pictures of time-dependent adsorption of polysulfides (Li_2S_4) by formamide (I), formamide with exfoliated LDH nanoflakes (II) and formamide with block LDHs (III), after (b) 0 min, (c) 1 min, (d) 5 min, (e) 40 min and (f) 12 h. (g) XRD pattern and (i) XPS spectrum of NiAl-LDHs after adsorption of Li_2S_4. (h) Structural diagram of self-assembled LDHs with Li_2S_4 in the interlayer space.

The black LDH precipitate formed by adsorbing Li_2S_4 was collected in an argon-filled glove box for XRD and XPS analyses. Figure 6g shows the XRD pattern of the precipitate, in which the diffraction peaks can be indexed to a NiAl-LDH type structure. The peak corresponding the *d*-spacing of 0.88 nm is indexed to the (003) planes and the peak with d = 0.15 nm is indexed to the (110) planes. It is reasonable that Li_2S_4 is converted into anions (*e.g.*, S_4^{2-}) in solution and then connects to the positively charged LDH nanoflakes by electrostatic interactions to form self-assembly of LDH/S_4^{2-} (Figure 6h). The variation of the c parameter of the composites with different anions is attributed to the volume difference among S_4^{2-}, NO_3^- and CO_3^{2-} (Figure S1).

The precipitate is further investigated by XPS. The peaks of Ni and Al (Figure S15) shift to higher binding energies after the adsorption of Li_2S_4, indicating a strong chemical affinity between LDH and Li_2S_4. Moreover, the peaks in the high-resolution S 2p XPS spectrum (Figure 6i) reflect four sulfur environments in the interlayers of LDHs. The double peaks at 163.2 and 164.4 eV are related to the bridging sulfur (S_B) of Li_2S_4, while the double peaks at 161.9 and 163.1 eV are associated with the terminal sulfur (S_T) of Li_2S_4.[6,48] The peaks at 166.7 and 168.7 eV correspond to thiosulfate and polythionate species, respectively, resulted from oxidation of Li_2S_4.[48] A significant phenomenon was found that LDH nanoflakes acted as a mediator to promote the conversion of LiPS. Some oxides were reported to have similar catalytic effects, such as $Ni(OH)_2$ and VO_2.[31,50] Thus, highly dispersed LDH nanoflakes in the structure of LDH/S/rGO can meet dual requirements for host material design, *i.e.*, a fast adsorption rate and strong adsorption capacity for LiPS. In a Li-S battery system, this is a more effective way to alleviate the shuttle effect of LiPS.

Theoretical simulations based on density functional theory (DFT) method are conducted to further explore the strong interaction between LDH nanoflakes and LiPS species. The relaxed structure of pristine NiAl-LDH is shown in Figure S16 with the lattice parameter of $a = b = 5.48$ Å. The geometry structure of polysulfides is distorted after being trapped by the LDH nanoflakes (Figure 7a1), indicative of a strong binding effect. It is widely believed that the stronger the binding strength, the better. The binding energies E_b of Li_2S_n (n =1, 2, 4, 6, 8) and sulfur adsorbed on LDH as the function of lithiation state are shown in Figure 7b. The binding strength roughly grows stronger with the increasing the lithiation state, except at Li_2S_2, where the binding energy drops from 6.28 eV of Li_2S_4 to 5.56 eV of Li_2S_2 when considering the vdW (van der Waals) corrections. It is worthy noticing that the binding energy for Li_2S_4 adsorption on LDH (6.28eV) is larger than on many other materials (Figure 7c). For example, the binding energies for the Li_2S_4 adsorption on Ni_3S_2[51] and most reported materials are smaller than 5.0 eV (with the vdW correction),[52] but the binding energy for the Li_2S_4 adsorption on LDH is 6.0 eV with the vdW correction. Even for the unlithiated S_8 adsorption on LDH, the binding energy (3.5 eV) is also much larger than those for the S_8 adsorption on many other materials (about 1.0 eV).[53] Such large binging energies indicate that Li_2S_n is strongly anchored on LDH, and the dissolution of intermediate Li_2S_n species into the electrolyte is severely blocked.

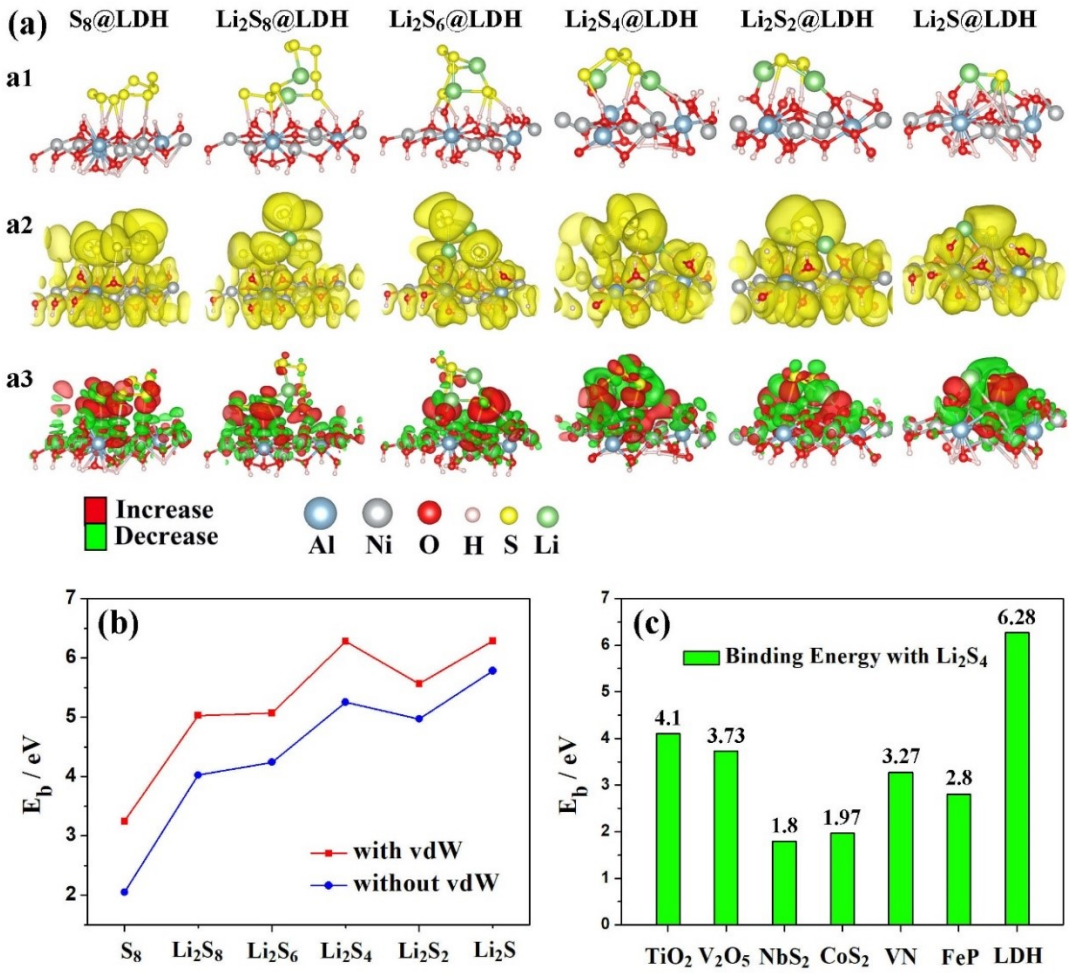

Figure 7. (a) Binding geometry configurations (a1), 3D representations of the ELF=0.5 isosurface (a2) and charge difference (a3) of different LiPS on the surface of a LDH nanoflake. (b) Binding energies between LDH and various polysulfides. (c) Binding energies of Li_2S_4 adsorbed on other host materials compared with that adsorbed on LDH.

Previously, Zhang *et al.* indicated that the interaction between the Li_2S_n species and 2D materials originates from the chemical binding between the Li atoms in the Li_2S_n species and the S (or O) atoms in the 2D layered materials.[52] It was clearly observed from the charge density difference (Figure 7a2) in our system that ionic bonds formed between the Li atoms (in the Li_2S_n) and the O atoms (in the LDH) because there is a net electron loss around the Li atoms and a net electron gain between the Li atoms and their adjacent O atoms in the LDH. Bader charge analysis

indicate that the O atoms have about 0.6 e acceleration after adsorption of Li_2S_n, and thus the Li atoms donate electrons to the O atoms.

In addition to the Li-O ionic bonding, there is also an interaction between the S atoms and the H atoms as the S atoms in the Li_2S_n species always come so close to the H atoms in LDH. We speculate that hydrogen bonds might form between the S atoms and the H atoms. There are only five kinds of interactions between atoms, and they are metal-bonds interaction, ionic-bonds interaction, covalent bonds interaction, vdW interaction, and H-bonds interaction. First, there is no metal atoms in the Li_2S_n species, and it is not possible to form metal-bonds between Li_2S_n and LDH. Second, charge density difference shows that the electrons decrease around the S-S bonds and increase around the S-H bonds, but Bader charge analysis indicates that the H atoms lose about only 0.2 e after adsorption on a monolayer (ML) LDH. The number of transferred electrons from H to S is so small that ionic bonds are not formed between these atoms. Third, the electron localization function (ELF) figures (Figure 7a3) show that there is no electron localization between the H atoms and the S atoms, thus they are not binding together through covalent bonds. Finally, the interaction between H in LDH and S in Li_2S_n is too strong to be attributed to the vdW interaction. The binding energy between Li_2S_n and ML LDH is larger than those of Li_2S_n adsorbed on many other materials[54,55] mainly due to the vdW interaction and ionic-bonds interaction between the Li atoms and the O atoms.[24] Besides, we also calculated the binding energies at different lithiation states without considering the vdW correction (Figure 7b). The binding strength without the vdW correction is still strong (larger than 2 eV), even for the unlithiated S_8, in which ionic interaction does not exist as the particles are Li-free. Thus, we concluded that S-H hydrogen bonds interaction is significant in between Li_2S_n and LDH. Additionally, Figure 7c show the binding energies of other host materials compared with LDH,[14,24,52,54,55] and obviously NiAl-LDH has the highest binding energy with Li_2S_4.

The good performance of LDH/S/rGO is attributed to the structural design (Figure 8). The existence of rGO in the crepe cake like structure not only improves the electron conductivity of the material, but also offers flexible space to tolerate the volume expansion of sulfur particles. In addition, the interaction between rGO and LDH is able to effectively hinder the self-assembly of LDH nanoflakes and raise the capture capability of LDH for LiPS. On the other hand, LDH nanoflakes, alternatively packing with the rGO layers into the crepe cake like structure, also plays an important role. The strong interaction between LDH and rGO nanosheets insures an all-round

packaged structure for sulfur particles, which can prevent the loss of sulfur, and improve the cycle life and stability of sulfur positive electrode. Furthermore, the intrinsic properties of LDH, such as positively charged and hydroxyl-rich surface present a strong affinity with LiPS.

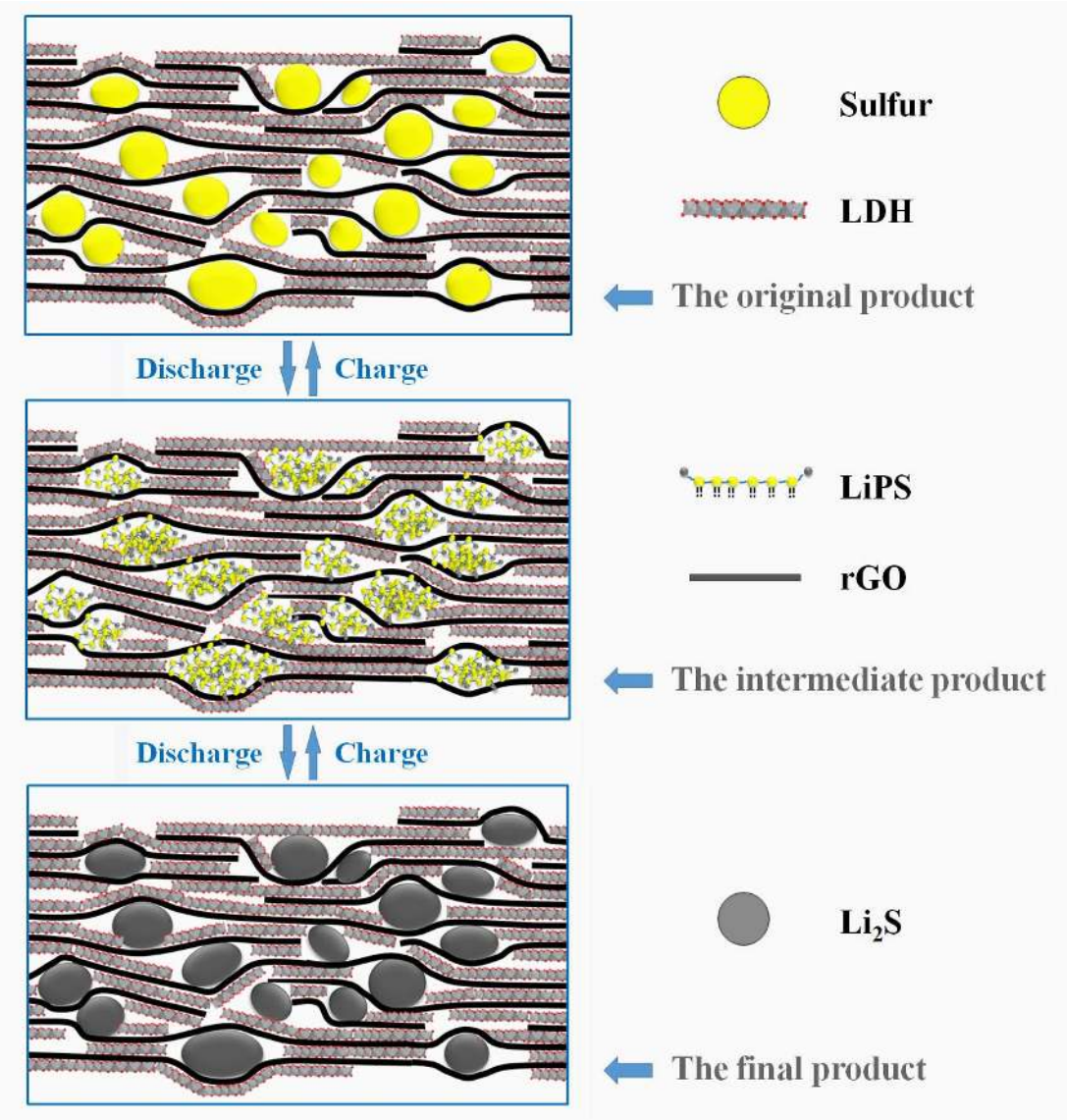

Figure 8. Schematic diagram of the phase transformation of the S-containing particles during the charge and discharge processes in the crepe cake like LDH/S/rGO. Flexible rGO layers act as a buffer for the volume change of sulfur particles.

The catalytic activity of LDH for conversion of LiPS is also favorable for hampering the escape of LiPS. More importantly, the sulfur particles maintain their nanoscale size in the confined space

in the crepe cake like structure and exhibit better electrochemical activity than bulk sulfur. Nanosized sulfur prefers to bond with lithium ion, which enhances the dynamics of sulfur positive electrode. In other words, the accelerated reaction kinetics would shorten the lifetime of LiPS and thereby improve the electrochemical performance of LDH/S/rGO.

CONCLUSION

In summary, we manipulate two kinds of 2D nanomaterials, positively charged LDH nanoflakes and negatively charged S-decorated rGO nanosheets, to form a crepe cake like structure *via* self-assembly. In this delicate design, the functionalization and stability of the electrode structure are taken into account. The construction relies on several strong interactions such as electrostatic force, polar interaction, Lewis acid-base bonding and hydrogen bonding. The sulfur nanocrystals are embedded and the shutter effect is minimized. As another important component, the flexible rGO layers provide fast electron transfer and buffer the volume expansion of sulfur in the charge and discharge processes. We also find that LDH can significantly accelerate the conversion of LiPS and reduce the positive electrode polarization in the redox process of sulfur, which enhance the overall specific energy and cycle life of the cell. This strategy for the design of electrode structure provides a concept for the development of high-performance Li-S batteries.

METHODS

Materials. Graphite (1000 M) was purchased from the Qingdao Jinhui Graphite Co., Ltd. Nickel nitrate ($Ni(NO_3)_2 \cdot 6H_2O$), aluminum nitrate ($Al(NO_3)_2 \cdot 6H_2O$), urea, sodium nitrate ($NaNO_3$), nitric acid (HNO_3), hydrochloric acid (HCl), formamide, sodium thiosulfate pentahydrate ($Na_2S_2O_3 \cdot 5H_2O$) were purchased from the Sinopharm Chemical Reagent Co., Ltd. All reagents are of analytical purity. Graphene oxide (GO) was synthesized by the modified Hummer's method.[41]

Preparation of S/rGO colloid solution. 0.12 g of graphene oxide was dispersed in 60 mL of deionized water by sonication for 2 h. 3.72 g of $Na_2S_2O_3 \cdot 5H_2O$ was then added into the GO colloid solution under magnetic stirring for 20 min. 100 mL of 0.3 M HCl was dropwise added into the above solution, followed by continuously magnetic stirring at 60 ℃ for 2 h to grow sulfur nanoparticles on the surface of GO nanosheets, and meanwhile GO was reduced to rGO.

Preparation of NiAl-LDH colloid solution. Highly crystalline NiAl-CO_3-LDHs (LDH/CO_3) were synthesized through a hydrothermal method. A mixed aqueous solution containing 0.58 g of

$Ni(NO_3)_2 \cdot 6H_2O$, 0.38 g of $Al(NO_3)_2 \cdot 6H_2O$ and 0.42 g of urea was transferred into a Teflon-lined autoclave and sealed in a steel container. The mixed solution was kept at 105℃ for 24 h. The product was recovered by centrifugation and washing with deionized water, followed by drying at 60 ℃ in an oven. Subsequently, to effectively exfoliate LDH, LDH/CO_3 was converted to LDH/NO_3 *via* ion exchange. Briefly, 0.4 g of LDH/CO_3 was added into 1 L of mixed solution consisting of 0.4 mmol HNO_3 and 0.4 mol $NaNO_3$. Note that the deionized water used for ion exchange should be boiled 10 min to remove CO_2 gas. The above solution was sealed to cut off outside air, and violently stirred for 24 h. The powder was vacuum filtered and purified by washing with deionized water. The as-synthesized LDH/NO_3 was obtained by vacuum drying at 80℃ for 10 h. 0.12 g of LDH/NO_3 was added into 150 mL of formamide in a beaker with sealing plug. LDH was exfoliated in formamide by using thermostatic mechanical shaking table at 25℃ for 24 h, when a blue colloid suspension was produced.

Preparation of LDH/S/rGO and LDH/rGO. LDH/S/rGO composite was prepared by self-assembly of exfoliated LDH and S-deposited rGO nanosheets. In a typical synthesis, the as-prepared LDH and S/rGO colloid suspensions were separately dropwise added into 50 mL of formamide in a beaker under magnetic stirring. After the dropping was completed, the brown mixed suspension was stirred for 1 h. Subsequently, 300 mL of deionized water was added into the mixed suspension under magnetic stirring for another 1 h. The LDH/S/rGO product was recovered by centrifugation at 5000 rpm and washing with deionized water, followed by a freeze-drying treatment. LDH/rGO was synthesized as a reference material by the same method except that S-free GO colloid suspension was used instead of S/rGO.

Theoretical calculation. The computations were carried out using DFT in the Vienna *ab initio* simulation package (VASP). The exchange correlation energy was described by the generalized gradient approximation (GGA) in the scheme proposed by Perdew–Burke–Ernzerhof (PBE). Van der Waals interaction was considered through the DFT-D3 approach. The projector-augmented wave (PAW) method was adopted with an energy cut-off of 400 eV in this study. Periodic boundary conditions were applied in all directions, and in order to avoid image-image interactions, a vacuum space of at least 15 Å between adjacent LDH layers was adopted. The structures of the monolayer (ML) LDH and polysulfides-LDH systems were firstly treated with conjugate gradient algorithm to relax the atomic position until the atomic forces were below 0.02 eV/Å. After successful completions of structure optimization, single point calculations were performed to

report the energies, and also to obtain the charge density difference and the electron localization function (ELF) in order to estimate the charge distribution situations. For this step, a k-mesh density of 0.02 $Å^{-1}$ under the Monkhorst-Pack method was sampled in the Brillouin zone. The binding energy was computed to measure the binding strength between the polysulfides and LDH, and can be defined as:

$$E_b = E_{Li2Sx+LDH} - E_{Li2Sx} - E_{LDH}$$

where $E_{Li2Sx+LDH}$, E_{Li2Sx}, E_{LDH} are the energies of the Li_2S_n-LDH combined system, the pure Li_2S_n, and pure LDH.

Materials characterization. Samples were initially characterized by XRD performed on a Phillips X'pert Pro MPD diffractometer with Cu Kα radiation. XPS was performed on a Shimadzu Axis Ultra spectrometer with an Mg Kα excitation source. Raman spectroscopy was performed on a Jobin-Yvon Laser Confocal Micro-Raman spectrometer with a 633 nm laser source. The thermogravimetric analysis (TGA) was carried out by a SDT Q600 (TA Instruments USA) thermal analyzer in a flow of N_2 at a heating rate of 10°C min^{-1} from 25 to 500°C. Samples were further investigated using SEM on a field emission scanning electron microscopy (FESEM, S-8010, Hitachi), scanning transmission electron microscopy (STEM) and HRTEM on a FEI Talos F200S electron microscope operated at 200 kV. The electron microscope is equipped with a high-angle annular dark-field (HAADF) detector, and energy dispersive X-ray spectroscopy (EDX) for elemental analysis.

Electrochemical measurements. The positive electrode was prepared by dropwise adding the ink onto the carbon paper (HCP030N, Hesen), and dried at 60°C in vacuum for 12 h. The ink was obtained by dispersing 80 wt% active material such as LDH/S/rGO, 10 wt% conductive carbon of super P and 10 wt% polyvinylidene difluoride (PVDF) in 1-methyl-2-pyrrolidinone (NMP). The mass loading of sulfur was about 2.5 mg cm^{-2}. 1:1 v/v DME and DOL solution containing 1 M lithium bis(tri-fluoromrthanesulfonyl)imide (LiTFSI) and 2 wt% $LiNO_3$ was used as the electrolyte, and lithium metal was used as the negative electrode. LR2032-type coin cells were assembled in an Ar-filled glove box (UniLab, Mbraun) prior to electrochemical measurements. The galvanostatic charge–discharge performance was measured by a LAND CT2001A test system at room temperature, and the voltage range was from 1.7 to 2.8 V (*versus* Li/Li^+). Cyclic voltammetry tests were done on a VMP3 electrochemical analyzer between 1.5 V and 3.2 V with a scan rate of 0.2 mV s^{-1}.

ASSOCIATED CONTENT

Supporting Information.

The Supporting Information is available free of charge at https://pubs.acs.org/doi/1xxxxxx.

Extended characterization including XRD patterns of NiAl-NO_3-LDHs, NiAl-CO_3-LDHs and LDH/S/rGO with different ratios of LDH : rGO; SEM-EDX mapping images of S/rGO and LDH/S/rGO; TEM-EDX mapping images of S/rGO and LDH/S/rGO after hundreds of cycles; TEM and HRTEM images of LDH/S/rGO before and after hundreds of cycles; high resolution XPS spectra of LDH/S/rGO and NiAl-LDHs/Li_2S_4; Raman spectra of GO and LDH/S/rGO; TGA curves of LDH/rGO, LDH/S/rGO, rGO and S/rGO; electrochemical measurements including rate performance of LDH/S/rGO and cycle performance of LDH/S/rGO with high areal sulfur loading and different ratios of LDH : rGO; The relaxed structure of pristine NiAl-LDH (PDF).

AUTHOR INFORMATION

Corresponding Authors

Wenbo Yue - Beijing Key Laboratory of Energy Conversion and Storage Materials, College of Chemistry, Beijing Normal University, Beijing 100875 (China); orcid.org/ 0000-0003-3809-6733; phone: +86-10-58804229; Email: wbyue@bnu.edu.cn

Jing Lu - State Key Laboratory for Mesoscopic Physics and Department of Physics, Peking University, Beijing 100871 (China); Email: jinglu@pku.edu.cn

Wuzong Zhou - School of Chemistry, University of St Andrews, St Andrews, Fife KY16 9ST (UK) ; Email: wzhou@st-andrews.ac.uk

Authors

Shengtang Liu - Beijing Key Laboratory of Energy Conversion and Storage Materials, College of Chemistry, Beijing Normal University, Beijing 100875 (China); orcid.org/ 0000-0002-1547-6605

Xiuying Zhang - State Key Laboratory for Mesoscopic Physics and Department of Physics, Peking University, Beijing 100871 (China)

Shitao Wu - School of Chemistry, University of St Andrews, St Andrews, Fife KY16 9ST (UK)

Xi Chen - Beijing Key Laboratory of Energy Conversion and Storage Materials, College of Chemistry, Beijing Normal University, Beijing 100875 (China); orcid.org/ 0000-0002-4018-0558

Xiaojing Yang - Beijing Key Laboratory of Energy Conversion and Storage Materials, College of Chemistry, Beijing Normal University, Beijing 100875 (China); orcid.org/ 0000-0003-3620-3507

Author Contributions

Shengtang Liu: Investigation, Methodology, Writing – Original Draft. **Xiuying Zhang:** Formal Analysis, Writing – Original Draft. **Shitao Wu:** Investigation. **Xi Chen:** Investigation, Validation. **Xiaojing Yang:** Supervision. **Wenbo Yue:** Conceptualization, Supervision, Funding Acquisition, Writing – Review & Editing. **Jing Lu:** Supervision, Formal Analysis, Funding Acquisition. **Wuzong Zhou:** Supervision, Writing – Review & Editing.

ACKNOWLEDGMENTS

This work was financially supported by National Natural Science Foundation of China (Nos. 21975030 and 11674005), and the Ministry of Science and Technology of China (No. 2016YFB0700600 (National Materials Genome Project)). The authors thank Yuri Andreev for useful discussions of the XRD studies of the composite specimens.

REFERENCES

(1) Pang, Q.; Liang, X.; Kwok, C. Y.; Nazar, L. F. Advances in Lithium-Sulfur Batteries Based on Multifunctional Cathodes and Electrolytes. *Nat. Energy* **2016**, *1*, 16132.

(2) Al Salem, H.; Babu, G.; Rao, C. V.; Arava, L. M. R. Electrocatalytic Polysulfide Traps for Controlling Redox Shuttle Process of Li-S Batteries. *J. Am. Chem. Soc*. **2015**, *137*, 11542-11545.

(3) Kong, L.; Chen, X.; Li, B.-Q.; Peng, H.-J.; Huang, J.-Q.; Xie, J.; Zhang, Q. A Bifunctional Perovskite Promoter for Polysulfide Regulation toward Stable Lithium-Sulfur Batteries. *Adv. Mater*. **2018**, *30*, 1705219.

(4) Song, Y.; Cai, W.; Kong, L.; Cai, J.; Zhang, Q.; Sun, J. Rationalizing Electrocatalysis of Li-S Chemistry by Mediator Design: Progress and Prospects. *Adv. Energy Mater*. **2019**, 1901075.

(5) Peng, H.-J.; Huang, J.-Q.; Cheng, X.-B.; Zhang, Q. Review on High-Loading and High-Energy Lithium-Sulfur Batteries. *Adv. Energy Mater.* **2017**, *7*, 1700260.

(6) Luo, D.; Li, G.; Deng, Y.-P.; Zhang, Z.; Li, J.; Liang, R.; Li, M.; Jiang, Y.; Zhang, W.; Liu, Y.; Lei, W.; Yu, A.; Chen, Z. Synergistic Engineering of Defects and Architecture in Binary Metal Chalcogenide toward Fast and Reliable Lithium-Sulfur Batteries. *Adv. Energy Mater.* **2019**, *9*, 1900228.

(7) Du, Z.; Chen, X.; Hu, W.; Chuang, C.; Xie, S.; Hu, A.; Yan, W.; Kong, X.; Wu, X.; Ji, H.; Wan, L.-J. Cobalt in Nitrogen-Doped Graphene as Single-Atom Catalyst for High-Sulfur Content Lithium-Sulfur Batteries. *J. Am. Chem. Soc*. **2019**, *141*, 3977-3985.

(8) Li, W.; Qian, J.; Zhao, T.; Ye, Y.; Xing, Y.; Huang, Y.; Wei, L.; Zhang, N.; Chen, N.; Li, L.; Wu, F.; Chen, R. Boosting High-Rate Li-S Batteries by an MOF-Derived Catalytic Electrode with a Layer-by-Layer Structure. *Adv. Sci.* **2019**, *6*, 1802362.

(9) Ji, X.; Lee, K. T.; Nazar, L. F. A Highly Ordered Nanostructured Carbon-Sulphur Cathode for Lithium-Sulphur Batteries. *Nat. Mater.* **2009**, *8*, 500-506.

(10) Chen, T.; Zhang, Z.; Cheng, B.; Chen, R.; Hu, Y.; Ma, L.; Zhu, G.; Liu, J.; Jin, Z. Self-Templated Formation of Interlaced Carbon Nanotubes Threaded Hollow Co_3S_4 Nanoboxes for High-Rate and Heat-Resistant Lithium-Sulfur Batteries. *J. Am. Chem. Soc*. **2017**, *139*, 12710-12715.

(11) Lv, X.; Wei, W.; Yang, H.; Li, J.; Huang, B.; Dai, Y. Group IV Monochalcogenides MX (M = Ge, Sn; X = S, Se) as Chemical Anchors of Polysulfides for Lithium-Sulfur Batteries. *Chem. - Eur. J.* **2018**, *24*, 11193-11199.

(12) Seh, Z. W.; Li, W.; Cha, J. J.; Zheng, G.; Yang, Y.; McDowell, M. T.; Hsu, P.-C.; Cui, Y. Sulphur-TiO_2 Yolk-Shell Nanoarchitecture with Internal Void Space for Long-Cycle Lithium-Sulphur Batteries. *Nat. Commun.* **2013**, 4, 1331.

(13) Liu, X.; Huang, J.-Q.; Zhang, Q.; Mai, L. Nanostructured Metal Oxides and Sulfides for Lithium-Sulfur Batteries. *Adv. Mater*. **2017**, 29, 1601759.

(14) Yuan, Z.; Peng, H.-J.; Hou, T.-Z.; Huang, J.-Q.; Chen, C.-M.; Wang, D.-W.; Cheng, X.-B.; Wei, F.; Zhang, Q. Powering Lithium-Sulfur Battery Performance by Propelling Polysulfide Redox at Sulfiphilic Hosts. *Nano Lett*. **2016**, *16*, 519-527.

(15) Ye, C.; Jiao, Y.; Jin, H.; Slattery, A. D.; Davey, K.; Wang, H.; Qiao, S.-Z. 2D MoN-VN Heterostructure to Regulate Polysulfides for Highly Efficient Lithium-Sulfur Batteries. *Angew. Chem. Int. Ed*. **2018**, *57*, 16703-16707.

(16) Sun, Z.; Zhang, J.; Yin, L.; Hu, G.; Fang, R.; Cheng, H.-M.; Li, F. Conductive Porous Vanadium Nitride/Graphene Composite as Chemical Anchor of Polysulfides for Lithium-Sulfur Batteries. *Nat. Commun.* **2017**, *8*, 14627.

(17) Li, Y.; Fang, J.; Zhang, J.; Yang, J.; Yuan, R.; Chang, J.; Zheng, M.; Dong, Q. A Honeycomb-Like Co@N-C Composite for Ultrahigh Sulfur Loading Li-S Batteries. *ACS Nano* **2017**, *11*, 11417-11424.

(18) Wang, H.; Zhang, W.; Xu, J.; Guo, Z. Advances in Polar Materials for Lithium-Sulfur Batteries. *Adv. Funct. Mater.* **2018**, *28*, 1707520.

(19) Xu, J.; Lawson, T.; Fan, H.; Su, D.; Wang, G. Updated Metal Compounds (MOFs, -S, -OH, -N, -C) Used as Cathode Materials for Lithium-Sulfur Batteries. *Adv. Energy Mater*. **2018**, *8*, 1702607.

(20) Su, D.; Cortie, M.; Fan, H.; Wang, G. Prussian Blue Nanocubes with an Open Framework Structure Coated with PEDOT as High-Capacity Cathodes for Lithium-Sulfur Batteries. *Adv. Mater.* **2017**, *29*, 1700587.

(21) Zheng, J.; Tian, J.; Wu, D.; Gu, M.; Xu, W.; Wang, C.; Gao, F.; Engelhard, M. H.; Zhang, J.-G.; Liu, J.; Xiao, J. Lewis Acid-Base Interactions between Polysulfides and Metal Organic Framework in Lithium Sulfur Batteries. *Nano Lett.* **2014**, *14*, 2345-2352.

(22) Seh, Z. W.; Sun, Y.; Zhang, Q.; Cui, Y. Designing High-Energy Lithium-Sulfur Batteries. *Chem. Soc. Rev*. **2016**, *45*, 5605-5634.

(23) Yuan, C.; Zhu, S.; Cao, H.; Hou, L.; Lin, J. Hierarchical Sulfur-Impregnated Hydrogenated TiO_2 Mesoporous Spheres Comprising Anatase Nanosheets with Highly Exposed (001) Facets for Advanced Li-S Batteries. *Nanotechnology* **2016**, *27*, 045403.

(24) Tao, X.; Wang, J.; Ying, Z.; Cai, Q.; Zheng, G.; Gan, Y.; Huang, H.; Xia, Y.; Liang, C.; Zhang, W.; Cui, Y. Strong Sulfur Binding with Conducting Magneli-Phase Ti_nO_{2n-1} Nanomaterials for Improving Lithium-Sulfur Batteries. *Nano Lett*. **2014**, *14*, 5288-5294.

(25) Chen, J.-J.; Yuan, R.-M.; Feng, J.-M.; Zhang, Q.; Huang, J.-X.; Fu, G.; Zheng, M.-S.; Ren, B.; Dong, Q.-F. Conductive Lewis Base Matrix to Recover the Missing Link of Li_2S_8 during the Sulfur Redox Cycle in Li-S Battery. *Chem. Mater.* **2015**, *27*, 2048-2055.

(26) Pang, Q.; Kundu, D.; Nazar, L. F. A Graphene-Like Metallic Cathode Host for Long-Life and High-Loading Lithium-Sulfur Batteries. *Mater. Horiz.* **2016**, *3*, 130-136.

(27) Wang, Q.; O'Hare, D. Recent Advances in the Synthesis and Application of Layered Double Hydroxide (LDH) Nanosheets. *Chem. Rev.* **2012**, *112*, 4124-4155.
(28) Zu, C.; Manthiram, A. Hydroxylated Graphene-Sulfur Nanocomposites for High-Rate Lithium-Sulfur Batteries. *Adv. Energy. Mater.* **2013**, *3*, 1008-1012.
(29) Jiang, J.; Zhu, J.; Ai, W.; Wang, X.; Wang, Y.; Zou, C.; Huang, W.; Yu, T. Encapsulation of Sulfur with Thin-Layered Nickel-Based Hydroxides for Long-Cyclic Lithium-Sulfur Cells. *Nat. Commun.* **2015**, *6*, 8622.
(30) Klein, M. J.; Veith, G. M.; Manthiram, A. Rational Design of Lithium-Sulfur Battery Cathodes Based on Experimentally Determined Maximum Active Material Thickness. *J. Am. Chem. Soc.* **2017**, *139*, 9229-9237.
(31) Dai, C.; Hu, L.; Wang, M.-Q.; Chen, Y.; Han, J.; Jiang, J.; Zhang, Y.; Shen, B.; Niu, Y.; Bao, S.-J.; Xu, M. Uniform Alpha-Ni$(OH)_2$ Hollow Spheres Constructed from Ultrathin Nanosheets as Efficient Polysulfide Mediator for Long-Term Lithium-Sulfur Batteries. *Energy Storage Mater.* **2017**, *8*, 202-208.
(32) Ge, X.; Gu, C.; Yin, Z.; Wang, X.; Tu, J.; Li, J. Periodic Stacking of 2D Charged Sheets: Self-Assembled Superlattice of Ni-Al Layered Double Hydroxide (LDH) and Reduced Graphene Oxide. *Nano Energy* **2016**, *20*, 185-193.
(33) Linghu, W.; Yang, H.; Sun, Y.; Sheng, G.; Huang, Y. One-Pot Synthesis of LDH/GO Composites as Highly Effective Adsorbents for Decontamination of U(VI). *ACS Sustainable Chem. Eng*. **2017**, *5*, 5608-5616.
(34) Zhou, D.; Cai, Z.; Lei, X.; Tian, W.; Bi, Y.; Jia, Y.; Han, N.; Gao, T.; Zhang, Q.; Kuang, Y.; Pan, J.; Sun, X.; Duan, X. NiCoFe-Layered Double Hydroxides/N-Doped Graphene Oxide Array Colloid Composite as an Efficient Bifunctional Catalyst for Oxygen Electrocatalytic Reactions. *Adv. Energy Mater.* **2018**, *8*, 1701905.
(35) Zhang, L.; Ji, L.; Glans, P.-A.; Zhang, Y.; Zhu, J.; Guo, J. Electronic Structure and Chemical Bonding of a Graphene Oxide-Sulfur Nanocomposite for Use in Superior Performance Lithium-Sulfur Cells. *Phys. Chem. Chem. Phys*. **2012**, *14*, 13670-13675.
(36) Yan, M.; Chen, H.; Yu, Y.; Zhao, H.; Li, C.-F.; Hu, Z.-Y.; Wu, P.; Chen, L.; Wang, H.; Peng, D.; Gao, H.; Hasan, T.; Li, Y.; Su, B.-L. 3D Ferroconcrete-Like Aminated Carbon Nanotubes Network Anchoring Sulfur for Advanced Lithium-Sulfur Battery. *Adv. Energy Mater*. **2018**, *8*, 1801066.

(37) Du, D.; Yue, W.; Fan, X.; Tang, K.; Yang, X. Ultrathin NiO/$NiFe_2O_4$ Nanoplates Decorated Graphene Nanosheets with Enhanced Lithium Storage Properties. *Electrochim. Acta* **2016**, *194*, 17-25.

(38) Guo, D.; Song, X.; Tan, L.; Ma, H.; Pang, H.; Wang, X.; Zhang, L. Hierarchical Structured Ni_3S_2@rGO@NiAl-LDHs Nanoarrays: A Competitive Electrode Material for Advanced Asymmetrical Supercapacitors. *ACS Sustainable Chem. Eng*. **2019**, *7*, 2803-2810.

(39) Yang, Z.; Ji, S.; Gao, W.; Zhang, C.; Ren, L.; Tjiu, W. W.; Zhang, Z.; Pan, J.; Liu, T. Magnetic Nanomaterial Derived from Graphene Oxide/Layered Double Hydroxide Hybrid for Efficient Removal of Methyl Orange from Aqueous Solution. *J. Col. Inter. Sci.* **2013**, *408*, 25-32.

(40) Wang, H.; Xiang, X.; Li, Feng. Facile Synthesis and Novel Electrocatalytic Performance of Nanostructured Ni–Al Layered Double Hydroxide/Carbon Nanotube Composites. *J. Mater. Chem.* **2010**, *20*, 3944-3952.

(41) Liu, S.; Zhang, C.; Yue, W.; Chen, X.; Yang, X. Graphene-Based Mesoporous SnO_2 Nanosheets as Multifunctional Hosts for High-Performance Lithium-Sulfur Batteries. *ACS Appl. Energy Mater.* **2019**, *2*, 5009-5018

(42) Zhou, W.; Chen, H.; Yu, Y.; Wang, D.; Cui, Z.; DiSalvo, F. J.; Abruna, H. D. Amylopectin Wrapped Graphene Oxide/Sulfur for Improved Cyclability of Lithium-Sulfur Battery. *ACS Nano* **2013**, *7*, 8801-8808.

(43) Xiao, P.; Bu, F.; Yang, G.; Zhang, Y.; Xu, Y. Integration of Graphene, Nano Sulfur, and Conducting Polymer into Compact, Flexible Lithium-Sulfur Battery Cathodes with Ultrahigh Volumetric Capacity and Superior Cycling Stability for Foldable Devices. *Adv. Mater*. **2017**, *29*, 1703324.

(44) Liu, D.; Zhang, C.; Zhou, G.; Lv, W.; Ling, G.; Zhi, L.; Yang, Q.-H. Catalytic Effects in Lithium-Sulfur Batteries: Promoted Sulfur Transformation and Reduced Shuttle Effect. *Adv. Sci.* **2018**, *5*, 1700270.

(45) Liu, Z.; Zhou, L.; Ge, Q.; Chen, R.; Ni, M.; Utetiwabo, W.; Zhang, X.; Yang, W. Atomic Iron Catalysis of Polysulfide Conversion in Lithium-Sulfur Batteries. *ACS Appl. Mater. Inter*. **2018**, *10*, 19311-19317.

(46) Huang, S.; Lim, Y. V.; Zhang, X.; Wang, Y.; Zheng, Y.; Kong, D.; Ding, M.; Yang, S. A.; Yang, H. Y. Regulating the Polysulfide Redox Conversion by Iron Phosphide Nanocrystals for High-Rate and Ultrastable Lithium-Sulfur Battery. *Nano Energy* **2018**, *51*, 340-348.

(47) Li, Z.; Zhang, J.; Lou, X. W. Hollow Carbon Nanofibers Filled with MnO_2 Nanosheets as Efficient Sulfur Hosts for Lithium-Sulfur Batteries. *Angew. Chem. Int. Ed*. **2015**, *54*, 12886-12890.
(48) Xiao, Z.; Yang, Z.; Li, Z.; Li, P.; Wang, R. Synchronous Gains of Areal and Volumetric Capacities in Lithium-Sulfur Batteries Promised by Flower-like Porous $Ti_3C_2T_x$ Matrix. *ACS Nano* **2019**, *13*, 3404-3412.
(49) Zheng, C.; Niu, S.; Lv, W.; Zhou, G.; Li, J.; Fan, S.; Deng, Y.; Pan, Z.; Li, B.; Kang, F.; Yang, Q.-H. Propelling Polysulfides Transformation for High-Rate and Long-Life Lithium Sulfur Batteries. *Nano Energy* **2017**, *33*, 306-312.
(50) Song, Y.; Zhao, W.; Zhu, X.; Zhang, L.; Li, Q.; Ding, F.; Liu, Z.; Sun, J. Vanadium Dioxide-Graphene Composite with Ultrafast Anchoring Behavior of Polysulfides for Lithium-Sulfur Batteries. *ACS Appl. Mater. Inter.* **2018**, *10*, 15733-15741.
(51) Li, Z.; Zhang, S.; Zhang, J.; Xu, M.; Tatara, R.; Dokko, K.; Watanabe, M. Three-Dimensionally Hierarchical $Ni/Ni_3S_2/S$ Cathode for Lithium-Sulfur Battery. *ACS Appl. Mater. Inter*. **2017**, *9*, 38477-38485.
(52) Zhang, Q.; Wang, Y.; Seh, Z. W.; Fu, Z.; Zhang, R.; Cui, Y. Understanding the Anchoring Effect of Two-Dimensional Layered Materials for Lithium-Sulfur Batteries. *Nano Lett*. **2015**, *15*, 3780-3786.
(53) Yin, L.; Liang, J.; Zhou, G.; Li, F.; Saito, R.; Cheng, H. Understanding the Interactions between Lithium Polysulfides and N-Doped Graphene Using Density Functional Theory Calculations. *Nano Energy* **2016**, *25*, 203-210.
(54) Ma, L.; Yuan, H.; Zhang, W.; Zhu, G.; Wang, Y.; Hu, Y.; Zhao, P.; Chen, R.; Chen, T.; Liu, J.; Hu, Z.; Jin, Z. Porous-Shell Vanadium Nitride Nanobubbles with Ultrahigh Areal Sulfur Loading for High-Capacity and Long-Life Lithium Sulfur-Batteries. *Nano Lett*. **2017**, *17*, 7839-7846.
(55) Chen, X.; Hou, T.; Persson, K. A.; Zhang, Q. Combining Theory and Experiment in Lithium-Sulfur Batteries: Current Progress and Future Perspectives. *Mater. Today* **2019**, *22*, 142-158.

For Table of Contents Only

A triphasic composite of layered double hydroxide/sulfur/reduced graphene oxide with a crepe cake like structure is designed and fabricated as a positive electrode material for Li-S batteries.